# Effects of infill patterns on the strength and stiffness of 3D printed topologically optimized geometries

Nadim S. Hmeidat

Mechanical, Aerospace and Biomedical Engineering Department, University of Tennessee, Knoxville, Tennessee, USA Bailey Brown, Xiu Jia and Natasha Vermaak

Mechanical Engineering and Mechanics Department, Lehigh University, Bethlehem, Pennsylvania, USA, and

Brett Compton

Mechanical, Aerospace and Biomedical Engineering Department, University of Tennessee, Knoxville, Tennessee, USA and Materials Science and Engineering Department, University of Tennessee, Knoxville, Tennessee, USA

#### **Abstract**

**Purpose** – Mechanical anisotropy associated with material extrusion additive manufacturing (AM) complicates the design of complex structures. This study aims to focus on investigating the effects of design choices offered by material extrusion AM – namely, the choice of infill pattern – on the structural performance and optimality of a given optimized topology. Elucidation of these effects provides evidence that using design tools that incorporate anisotropic behavior is necessary for designing truly optimal structures for manufacturing via AM.

**Design/methodology/approach** – A benchmark topology optimization (TO) problem was solved for compliance minimization of a thick beam in three-point bending and the resulting geometry was printed using fused filament fabrication. The optimized geometry was printed using a variety of infill patterns and the strength, stiffness and failure behavior were analyzed and compared. The bending tests were accompanied by corresponding elastic finite element analyzes (FEA) in ABAQUS. The FEA used the material properties obtained during tensile and shear testing to define orthotropic composite plies and simulate individual printed layers in the physical specimens.

Findings – Experiments showed that stiffness varied by as much as 22% and failure load varied by as much as 426% between structures printed with different infill patterns. The observed failure modes were also highly dependent on infill patterns with failure propagating along with printed interfaces for all infill patterns that were consistent between layers. Elastic FEA using orthotropic composite plies was found to accurately predict the stiffness of printed structures, but a simple maximum stress failure criterion was not sufficient to predict strength. Despite this, FE stress contours proved beneficial in identifying the locations of failure in printed structures.

Originality/value — This study quantifies the effects of infill patterns in printed structures using a classic TO geometry. The results presented to establish a benchmark that can be used to guide the development of emerging manufacturing-oriented TO protocols that incorporate directionally-dependent, process-specific material properties.

Keywords Anisotropy, Additive manufacturing, Finite element analysis, 3D printing, Topology optimization

Paper type Research paper

#### 1. Introduction

Material extrusion additive manufacturing (AM) processes, such as fused filament fabrication (FFF), big area additive manufacturing and direct-ink writing, build three-dimensional (3D) components by depositing extruded filaments of material from a nozzle mounted on a computer-controlled, multi-axis motion stage. The path that the nozzle takes while depositing material filaments – also known in the literature as "roads" or "infill roads" – is referred to as a "print path." For most printed components, any given layer may be printed using a variety of print path options (Agarwala et al., 1996). The collection of

print paths that make up a given structure will be referred to as the "infill pattern." The specific choice of print path and infill pattern can have profound implications for the performance of the printed component due to anisotropy that may arise as a result of the print path and the nature of material extrusion AM. For traditional polymer FFF processes, anisotropy is primarily associated with a weak bond between successive deposition print paths (Ahn et al., 2002; Bellini and Güçeri, 2003; Sun et al., 2008), while material extrusion AM of composite materials brings the added complexity that filler materials partially or fully orient along the print direction

The current issue and full text archive of this journal is available on Emerald Insight at: https://www.emerald.com/insight/1355-2546.htm



This work is supported by the National Science Foundation (NSF) under Grant No. CMMI-1825815. The authors would also like to thank Mr Jake Dvorak and Mr Zane Palmer for assistance preparing test specimens and Dr Stephen Young and Mr Zach Arwood for assistance with shear tests.

Received 21 April 2020 Revised 19 December 2020 Accepted 28 February 2021

(Calvert et al., 1997; Compton and Lewis, 2014; Duty et al., 2017; Hmeidat et al., 2018; Peng et al., 1999; Pierson et al., 2019; Shofner et al., 2003; Tekinalp et al., 2014; Grejtak et al., 2020; Trigg et al., 2021). In this case, the anisotropy in a printed composite component may be the result of a combination of intrinsic material anisotropy and extrinsic bonding-related anisotropy. Recently, Hmeidat et al. (2020) reported mechanical anisotropy in printed epoxy nanocomposites containing high-aspect-ratio filler materials with varying nozzle size, print speed and print path orientation. To mitigate or leverage the anisotropy inherent in material extrusion AM, and to enable the application of rigorous engineering principles to mechanical design for material extrusion AM, it is necessary to develop a more complete understanding of how print path, infill pattern and associated anisotropy affects strength, stiffness and failure modes in complex geometries, such as those resulting from topology optimization (TO).

TO has emerged as a leading design tool to leverage the freedom that AM processes afford compared to conventional manufacturing methods (Liu et al., 2018). TO is a method of designing structures with the most efficient material distribution for a given set of constraints, objectives and loading. TO often yields designs that are geometrically complex and difficult or impossible to manufacture with traditional machining or casting. At the same time, there has been significant progress made toward tailoring TO to address the characteristic strengths and/or limitations of particular AM processes. For example, TO and the design of support-free structures have been investigated for two-dimensional applications by Leary et al. (2014) and 3D applications by Langelaar (2016). Minimum feature size and manufacturability constraints were addressed by Lazarov et al. (2016) and Allaire et al. (2016) among many others (Liu et al., 2018; Liu and Ma, 2016). To include AM infill parameters and directionality in manufacturing-oriented TO, Liu and Yu (2017) proposed a concurrent level-set TO and deposition path planning protocol, which was subsequently expanded for 3D applications with a self-support constraint (Liu and To, 2017). Jiang et al. (2019) proposed print path planning for AM with fiber-reinforced composites and Wu et al. (2017) created an infill optimization protocol for porous AM structures. Cheng et al. (2017) presented an optimization protocol for variable density AM cellular structures, along with experimental validation. Gaynor et al. (2014) used the multi-material capabilities of Polyjet 3D printers to manufacture optimized three-phase compliant mechanisms.

While there has been explosive growth in the development of manufacturing-oriented TO, the benchmark experimental quantification of the choice of discrete print paths on performance-based quantities of interest, such as strength, stiffness and failure modes, is lacking. Jiang et al. (2019) experimentally measured the stiffness of composite polylactic acid (PLA)/carbon fiber beams that were optimized for fiber orientation. Yang et al. (2018) evaluated the effect of stereolithography printing build direction on the stiffness of TO designs. However, further research is required to characterize the effect of print path on not only stiffness but also strength and failure modes exhibited by FFF structures identified by

TO. These types of studies may inform better decisions about if, when and how to capitalize on AM design freedom.

In this study, we consider a benchmark example of a beam optimized for stiffness under three-point bending. The beam structure is generated using TO and printed using a variety of infill pattern strategies to characterize the effects of print path on the stiffness, strength and failure behavior in a complex beam structure. The paper is organized as follows: In Section 2, we present the TO method used to determine the optimized beam design for this study; in Section 3, experimental and numerical methods are outlined for the creation of the test specimens, mechanical characterization (including tensile, shear and bending tests) and finite element analysis (FEA); experimental and numerical results are presented in Section 4, followed by analysis and discussion in Section 5. Section 6 concludes the paper.

# 2. Topology optimization

TO is a method of determining the most efficient material distribution within a design domain for a structure given the objective function and a set of constraints (Bendsøe and Sigmund, 2004). This method has been applied to a wide variety of applications, including but not limited to structural compliance (Bendsøe, 1989), heat conduction (Gersborg-Hansen et al., 2006) and vibrations/dynamic response (Ma et al., 1993). The principles of TO have been applied with a variety of approaches, including homogenization (Bendsøe and Kikuchi, 1988), level set (Wang et al., 2003; Allaire et al., 2004), density-based methods (Bendsøe, 1989) and others (Sigmund and Maute, 2013; Deaton and Grandhi, 2014).

Solid isotropic material with penalization (SIMP) is one of the most widely used density-based approaches for TO. In SIMP, a relative density is assigned to each element in a discretized design domain. The element densities,  $\rho_e$ , which vary from 0 (void) to 1 (solid material), are treated as design variables in the optimization and are used to establish the distribution of material within the structure. The material properties within an element are assumed to be constant and are determined as a function of the relative density of the element raised to some penalization factor (here, p = 3), which serves to discourage the formation of elements with intermediate densities.

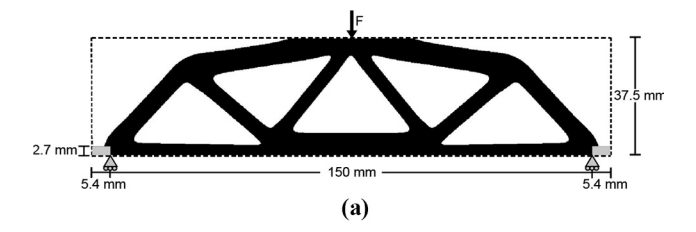
This study focuses on a two-dimensional benchmark structural compliance optimization problem for a beam under three-point bending (Figure 1) (Bendsøe and Sigmund, 2004), using the 88-line code from Andreassen *et al.* (2011). The 88-line code is a standard educational instrument that is recognized as a basis or benchmark for new developments in the field of TO (Andreassen *et al.*, 2011). The problem for the compliance minimization ( $C(\rho)$ ) can be stated:

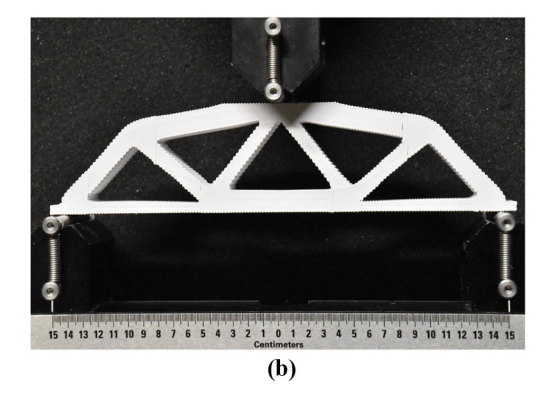
$$\frac{\min}{\rho} \quad C(\rho) = \quad \boldsymbol{U}^T \boldsymbol{K} \boldsymbol{U} = \sum_{e=1}^{N} \rho_e^{\ p} u_e^T k_e u_e$$

s.t. 
$$\frac{\sum \rho_e}{V_0} < f$$
;  $KU = F$ ;  $0 < \rho_{min} \le \rho_e \le 1$ 

where K, U, F and  $\rho$  are the global stiffness matrix, nodal displacement vector, force vector and density matrix, respectively;

**Figure 1** (a) Optimization results for the compliance minimization of a beam under three-point bending. The design domain, referenced by the dashed line, included  $1,080 \times 252$  elements. The gray non-optimizable tabs were defined explicitly to be solid to facilitate experimental setup, as shown in (b)





 $k_e$ ,  $u_e$  and  $\rho_e$  are the element stiffness matrix, nodal displacement vector and density, respectively;  $V_0$  is the volume of the design domain; f is the target volume fraction; and  $\rho_{min} = 10^{-9}$  is the minimum relative density.

In this optimization, the rectangular design domain was discretized into  $1,080 \times 252$  square elements. Rectangular tabs of material (18 x 36 elements in size) were prescribed on the outer boundary of the structure to facilitate support conditions. The target volume fraction was defined as f = 0.4. The results of this standard beam compliance problem (Figure 1) serve as the basis for comparing the effects of printing decisions on the actual performance and observed failure mechanisms in the optimized geometry.

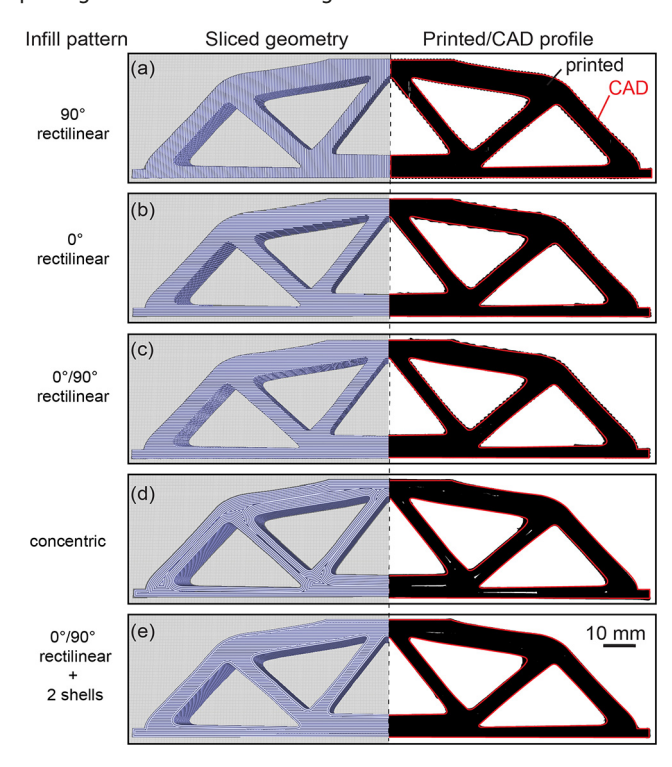
# 3. Methods

# 3.1 Sample fabrication

A computer-aided design (CAD) model of the optimized geometry (Figure 1) was generated by transforming the density field obtained by TO to an stereolithography (STL) file using a MATLAB code (Liu and Tovar, 2014). The STL file was then imported into SolidWorks 2018 for manual manipulation to smooth some jagged edges within the optimized geometry. The CAD model was then sliced using the open source software Cura LulzBot Slicer, version 3.2.32 (www.lulzbot.com/cura) using the following discrete infill patterns:

- 90° rectilinear pattern, in which all printed roads are laid down orthogonal to the length of structure (Figure 2a).
- 0° rectilinear pattern, in which all printed roads are laid down parallel to the length of the structure (Figure 2b).
- 0°/90° rectilinear pattern, in which the 0° rectilinear and 90° rectilinear infill pattern alternate between layers (Figure 2c).

**Figure 2** Sliced and printed optimal geometries with different discrete infill patterns. Left: sliced geometry. Right: corresponding printed surfaces. The CAD geometry (shown in red) is overlaid on the scanned printed surfaces to evaluate geometric fidelity. The porosity because of printing is shown in white in the right column



 Concentric pattern, in which all printed roads are laid down parallel to the perimeter of the structure (Figure 2d). All infill patterns used were available in the printer settings.

All specimens in this study were additively manufactured using a LulzBot TAZ 6 FFF printer (Aleph Objects, Inc., CO, USA) with a 0.5 mm brass nozzle. The material used was acrylonitrile butadiene styrene (ABS) (Chroma Strand Lab), with a filament size of 2.85 mm. All specimens were printed under the same print parameters that are summarized in Table 1.

The infill patterns (Figure 2) were first printed without incorporation of shells (i.e. perimeters or walls). However, to investigate how the use of shells affects the design's structural performance and geometric fidelity, additional samples using only the  $0^{\circ}/90^{\circ}$  rectilinear infill patterns were printed with two

Table 1 Print parameters

Print parameters	Corresponding value			
Bed temperature (°C)	110			
Print-head temperature (°C)	245			
Layer height (mm)	0.38			
Filament spacing (mm)	0.5			
Infill percentage (%)	100			
Extrusion factor (%)	100			
Wall print speed (mm/s)	30			
Infill print speed (mm/s)	55			

(Figure 2e) and four shells. All printed optimized geometries had an average thickness of ~18.8 mm (49 layers). As a baseline for comparison, the optimized geometry was also waterjet-cut from an ABS bulk sheet (McMaster-Carr, Elmhurst, IL) of the same thickness as the printed designs. However, it should be noted that the bulk sheet was made out of a different ABS grade than the ABS filaments used for printing. The weight measurements of all printed geometries are summarized in Table 2. Figure 3 shows high magnification optical micrographs of regions from the bulk (Figure 3a) and printed (Figures 3 b-g) optimized structures.

The infill patterns used in this study were deliberately chosen to encapsulate the conceptual extremes and more realistic, practical infill patterns available. While uniform, rectilinear infill patterns (such as the 0° and 90° rectilinear patterns) are not commonly used, they are useful in clearly identifying some useful insights that can be applied more broadly when making design choices for AM. More practical infill patterns (i.e. 0°/90° rectilinear and concentric) were included as well. Because these infill patterns more closely reflect standard printing practices, it is useful to investigate the effects of the inclusion of shells, which is also fairly standard practice. 0°/90° rectilinear specimens were, therefore, printed with and without shells (the concentric infill pattern essentially already includes shells).

To evaluate the geometric fidelity of the printed optimized geometries, the profile area associate with each sample was measured and compared with the profile area of the original CAD model. The profile area of the printed structures was scanned using an optical scanner (Brother Industries, Ltd) and the scans were then converted into black and white binary images using the open source image processing software *Image*?, version 1.52a (available at: http://imagej.nih.gov/ij).

Tensile and shear specimens were waterjet-cut from 100 mm x 100 mm x 3.2 mm sheets that were printed using the same

parameters given in Table 1. The dimensions of the tensile specimens were selected according to American Society for Testing and Materials (ASTM) D638 (Standard, 2010), using type V and the shear specimens according to ASTM D5379 (Standard, 2005), using the V-notched beam method. The shear specimens were waterjet-cut from the printed sheets in the form of rectangular beams, and then were notched via machining. Two material orientations were used for both types of test specimens.

In this study, coordinate systems will be referred to using the following convention: the 1-3 coordinates refer to a local coordinate system that corresponds to the material orientation with 1 denoting the longitudinal direction (parallel to the translation of the print head), 2 denoting the in-plane transverse direction and 3 denoting the out-of-plane direction. The x, y and z coordinates refer to a global coordinate system as illustrated in Figure 4.

#### 3.2 Mechanical characterization

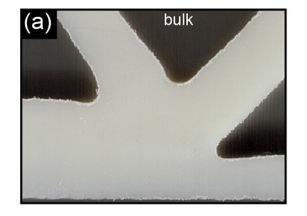
All mechanical tests were conducted at ambient lab temperature. The printed structures were tested in three-point bending on an electromechanical load frame (Model 45, MTS Systems Corporation, Eden Prairie, MN, USA) using a 10 kN load cell and a span-length of 150 mm, as illustrated in Figure 1b. A crosshead speed of 0.9 mm/min was used. A time-lapse video was recorded during the tests to analyze the progression of failure events. For the bulk and each infill pattern used, three optimized structures were tested in three-point bending.

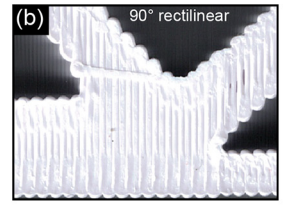
The tensile tests were also conducted on the aforementioned load frame and load cell. A head-rate of 1 mm/min was used following ASTM D638 (Standard, 2010), resulting in a strain rate of 0.0022 1/s. The shear tests were performed on a servohydraulic load frame (858 Table Top System, MTS Systems Corporation, Eden Prairie, MN, USA) using a 25 kN load cell and a crosshead speed of 2 mm/min. A 3D digital

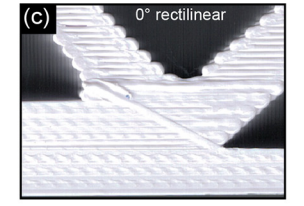
Table 2 Infill pattern, geometric error and weight of printed optimized geometries

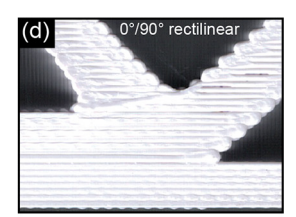
Infill pattern	Bulk	90° rectilinear	0° rectilinear	0°/90° rectilinear	Concentric	0°/90° two shells	0°/90° four shells
Geometric error (%) Weight (g)	$3.2 \pm 0.10$ $46.6 \pm 0.19$	$8.1 \pm 0.08$ $48.5 \pm 0.19$	$8.2 \pm 0.63$ $48.3 \pm 0.23$	$7.9 \pm 0.09 \\ 48.5 \pm 0.03$	$4.4 \pm 0.42 \\ 47.5 \pm 0.09$	$3.8 \pm 0.58$ $48.1 \pm 0.0$	4.9 ± 0.04 48.0 ± 0.06

Figure 3 High-magnification optical images of regions from the bulk and printed structures with different infill patterns

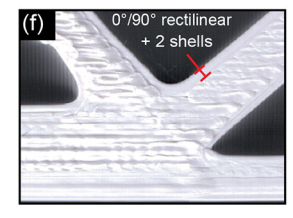












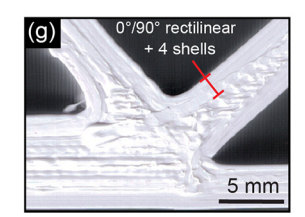


**Figure 4** Boundary and loading conditions for the one-quarter numerical mode, using symmetry. Detail boxes show examples of the different infill pattern cases

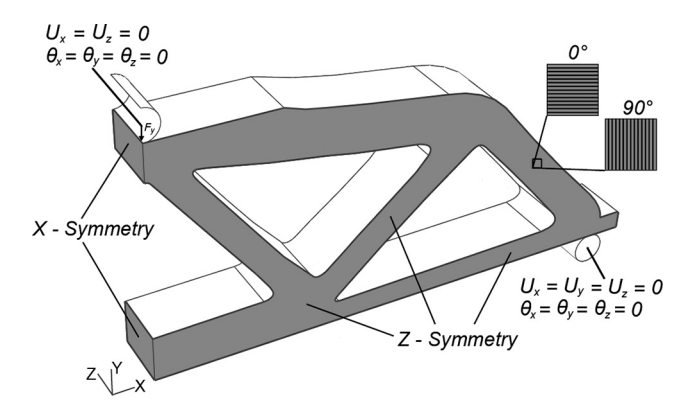


image correlation (DIC) system (Correlated Solutions, Inc) was used during both tensile and shear tests to measure strain fields. Poisson's ratio was extracted from the tensile test results by applying virtual strain gauges within the gauge-length of the specimen (7.62 mm), using VIC-2D software (Correlated Solutions, Inc). One virtual gauge was used to measure strains in the direction parallel to the applied load, and the other for strains in the transverse direction. A minimum of five specimens per material orientation was used for the tensile tests and three specimens for the shear tests. The relevant Poisson's ratios are defined relative to the material orientations as follows:

$$u_{12} \equiv \frac{-\varepsilon_{22}}{\varepsilon_{11}}, 
u_{21} \equiv \frac{-\varepsilon_{11}}{\varepsilon_{22}}$$

where  $\varepsilon_{11}$  and  $\varepsilon_{22}$  are the normal strains and  $\nu_{11}$  and  $\nu_{21}$  are the Poisson's ratios. Subscripts refer to material orientations (Section 3.1).

# 3.3 Finite element analysis

To aid interpretation of the three-point bending experiments and rationalize the observed failure behaviors, quasi-static structural simulations of the bending experiments were conducted using the commercial finite element software ABAQUS 2018 (SIMULIA, Providence, RI). For all simulations, a 3D quarter-symmetry model shown in Figure 4 was used with nonlinear geometric effects included. The mesh consisted of 23,058 solid hexahedral elements (based on the results of a mesh sensitivity analysis). Cylindrical, analytical rigid surfaces were used to represent the 5-mm-diameter steel supports from the experimental setup (Figure 1b). The analytical surfaces were placed in hard, frictionless contact with the beam.

To approximate the effects of the discrete infill patterns in the printed structures, appropriate in-plane orthotropic elastic properties and material orientations were defined for each infill pattern:  $90^{\circ}$  rectilinear,  $0^{\circ}$  rectilinear,  $0^{\circ}/90^{\circ}$  rectilinear and concentric. The properties were defined based on the testing outlined in Section 3.2 and refer to material orientations defined at the end of Section 3.1. The 3-direction properties were assumed to be the same as the properties in the 2-direction. In the  $0^{\circ}$  case, the 1-direction

was aligned with the x-axis and in the  $90^{\circ}$  case, it was aligned with the y-axis (Figure 4). In the  $0^{\circ}/90^{\circ}$  case, alternating layers of 0° and 90° in-plane print paths were used to build the structure. This case was modeled with the use of a composite lay-up module in ABAOUS, with 49 alternating plies serving to represent the alternating 49 layers in the printed specimens. In the concentric case, the 1-direction remained tangent to the perimeter, and thus, changed continuously throughout the structure. To model this case, the material orientation was discretely defined for each element to be tangent to the closest perimeter edge, as illustrated in Figure 5. Although this approach does not exactly match the experimental concentric infill patterns, comparison to the printed sample indicates that the numerical model broadly captures the salient features of the experimental sample. A simulation approximating the water-jet cut bulk ABS geometry was conducted using the material properties measured from the bulk ABS tensile and shear tests (Table 3). Finally, two additional isotropic simulations were performed using isotropic material properties representative of the 1- and 2-directions, respectively. These simulations were used to provide bounding behavior for the orthotropic simulations, as well as providing a means of direct comparison with the FEA simulations using the orthotropic elastic properties of printed ABS and material orientations for each printed infill pattern.

In the simulations, a load of 3 kN was applied to the loading pin (also modeled with a rigid analytical surface). Output data was recorded for fixed intervals of 30 N to have sufficient resolution for comparison with the experiments. From these numerical results, values for the structural stiffness and theoretical failure load were obtained. Failure in the elastic simulations was assumed to occur once the direct stresses at any location exceeded the tensile or shear strength,  $\sigma_{ult,11}$ ,  $\sigma_{ult,22}$  or  $\sigma_{ult,21}$ , respectively, that was measured in the tensile and shear tests (Section 3.2). The load at which this occurred in the simulations was defined as the failure load for that case. In

**Figure 5** (a) The actual printed concentric infill pattern. (b) The concentric infill pattern illustrated for the first layer of half of the optimized design

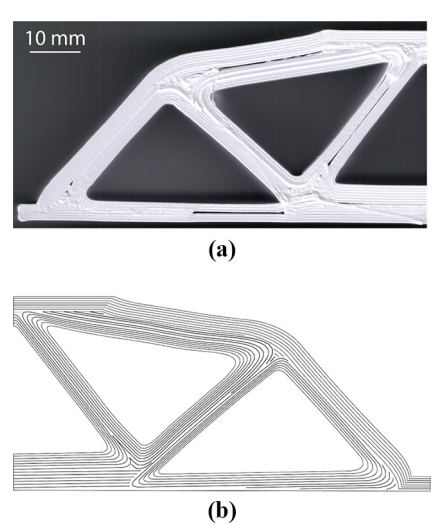


**Table 3** Tensile and shear properties of bulk and printed coupons

Test direction	Ultimate strength (MPa)	Young's modulus (GPa)	Poisson's ratio	Shear strength (MPa)	Shear modulus (GPa)
Bulk	26.8 ± 3.1	$1.82 \pm 0.04$	$0.36 \pm 0.01$	27.3 ± 2.8	$0.79 \pm 0.01$
1-direction	$34.3 \pm 2.0$	$2.41 \pm 0.08$	$\textbf{0.36} \pm \textbf{0.01}$	$27.3 \pm 0.6$	$0.82 \pm 0.03$
2-direction	$17.3 \pm 2.4$	$1.93 \pm 0.06$	$0.25\pm0.02$	$23.0 \pm 0.4$	$\textbf{0.83} \pm \textbf{0.04}$

the  $0^{\circ}/90^{\circ}$  case, each ply in the structure was checked for failure, using an average of the 1-direction and 2-direction tensile ultimate strengths (Table 3) as the failure strength.

# 4. Results

#### 4.1 Geometric fidelity

Figure 2 compares the sliced geometry (left-hand column) and the profile of the printed geometries (middle column), along with corresponding detail regions that show the infill pattern within the physical specimens (right-hand column). Geometric error is summarized in Table 2. All the infill patterns and the bulk, water jet cut samples, resulted in printed geometries that were larger than the source CAD model. The CAD profile area is outlined in red in Figure 2. The  $90^{\circ}$  rectilinear,  $0^{\circ}$  rectilinear cases result in a geometric error of  $\sim 8\%$ , while structures that use shells result in geometric error of  $\sim 4\%$ . The bulk, waterjet-cut structure results in a geometric error of 3.2%, indicating that the waterjet process has removed less material than prescribed in the CAD model.

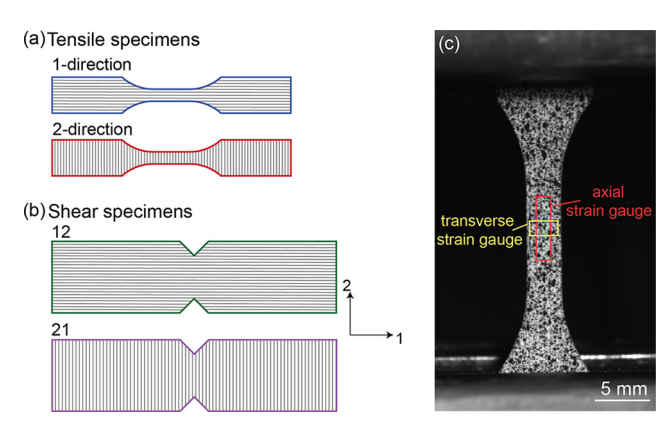
When shells are not included, the end of trajectories, where the print head makes a U-turn, often pass beyond the targeted printing domain specified in the CAD model, which results in a larger printed profile area. This phenomenon is referred to as the stair-stepping effect or discretization, which occurs naturally as a result of stacking layers during printing, causing visible "stair steps" or curved features (Gibson *et al.*, 2014). This can be clearly observed in the detailed views given in Figures 3b–d. When shells are present, they act as boundaries that define the geometry and enclose the infill pattern, resulting in a higher geometric fidelity. The shells are typically added to improve accuracy and surface finish in printed parts (Gibson *et al.*, 2014).

In the case of the concentric infill pattern, large pores can occur in the central region of the geometry where print paths originating from opposing sides of the geometry meet. If the central gap is smaller than the width of two additional print paths, the gap will remain unfilled, leaving a large, high-aspectratio pore. Examples of this phenomenon are visible in Figures 2d and 3e.

#### 4.2 Tensile and shear properties

Figures 6a–b show schematic illustrations of the test specimens used for both tensile and shear tests, respectively. Representative stress-strain plots of the tensile and shear tests are shown in Figure 7 and the corresponding mechanical properties are summarized in Table 3. The ultimate tensile strength in the 1-direction is  $34.3 \pm 2$  MPa, and the ultimate tensile strength in the 2-direction is  $17.3 \pm 2.4$  MPa (Figure 7a). The failure, in this case, occurs along the interface between individual print paths with little inelastic deformation. The bulk

**Figure 6** Schematic illustrations of (a) tensile specimens and (b) shear specimens with different material orientations. (c) Tensile test setup along with the speckle pattern used for DIC measurements, as well as virtual strain gauges in both axial and transverse directions applied to extract Poisson's ratio



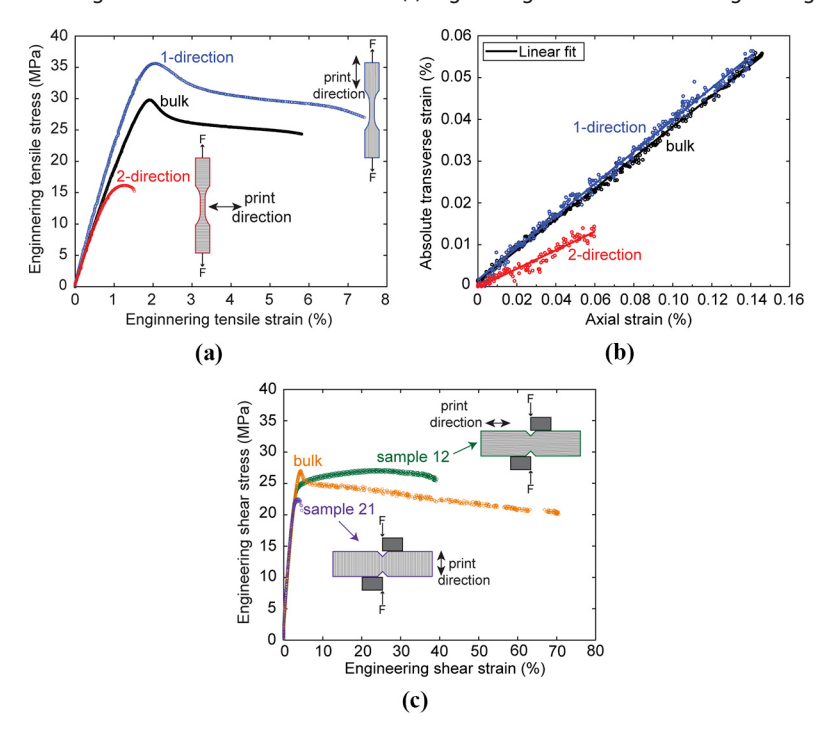
sample exhibits an ultimate tensile strength of  $26.8 \pm 3.1$  MPa. To calculate Poisson's ratio, the axial and transverse strains from the elastic region of deformation were extracted by DIC during the tensile tests and plotted against each other (Figure 7b). Poisson's ratio is then given by the slope of the resulting line. Slopes were computed using linear regression (solid lines in Figure 7b) and the calculated average Poisson's ratios are  $0.36 \pm 0.01$  and  $0.25 \pm 0.02$  for  $\nu_{12}$  and  $\nu_{21}$ , respectively. The Poisson's ratio of the bulk sample is identical to  $\nu_{12}$ . Schematic illustrations of the printed tensile specimens are shown in Figure 7a for 1-direction and two-direction specimens.

Figure 7c shows the shear response of the printed coupons tested in two orthogonal material orientations. As expected, the elastic response is identical, but differences arise with the onset of large strains and inelastic deformation. When the interface between print paths is oriented vertically from notch tip to notch tip, failure propagates along the print path interface, leading to complete failure at low shear strain. However, when the print path interface is oriented horizontally, such interfacial failure is not catastrophic and large inelastic shear strains can be supported. The average ultimate shear strength values for this material are  $27.3 \pm 0.6$  and  $23 \pm 0.4$  MPa, for  $\tau_{12}$  and  $\tau_{21}$ , respectively. The average ultimate shear strength of the bulk sample is  $27.3 \pm 2.8$  MPa. Schematic illustrations of the printed shear specimens are shown in Figure 7c for Samples 12 and 21.

#### 4.3 Printed structures

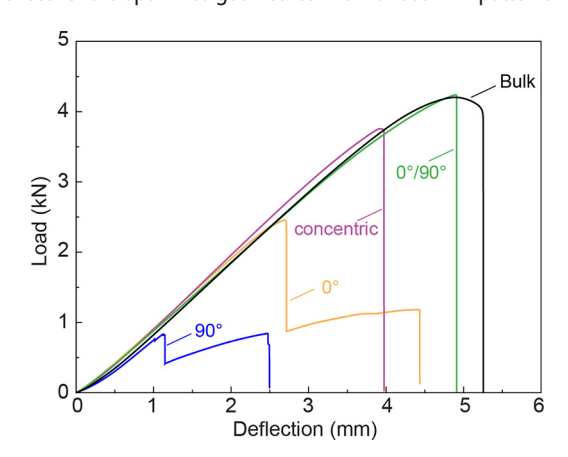
Representative experimental load-deflection curves of the optimized structure with different infill patterns and the bulk case are displayed in Figure 8. The  $90^{\circ}$  rectilinear pattern has the

**Figure 7** Representative plots of (a) engineering tensile stress versus engineering tensile strain, (b) axial versus transverse strain (absolute values) measured from DIC during tensile testing to determine Poisson's ratio and (c) engineering shear stress versus engineering shear strain



poorest performance, with a stiffness of  $0.89 \pm 0.03$  kN/mm, and an initial failure load of  $0.95 \pm 0.12$  kN, followed by a secondary failure event at  $0.92 \pm 0.14$  kN (blue line in Figure 8). Similarly, the  $\theta$ ° rectilinear pattern exhibits two failure events, but at higher failure loads of  $2.1 \pm 0.31$  kN and  $1.22 \pm 0.074$  kN for the primary and secondary failure events, respectively (yellow line in Figure 8). The  $\theta$ ° rectilinear pattern is also stiffer at  $0.99 \pm 0.01$  kN/mm. All other infill patterns and the bulk case, fail in one single event at significantly higher loads. The concentric pattern fails at  $3.8 \pm 0.06$  kN (purple line in Figure 8), followed by the  $\theta$ °/ $\theta$ 0° rectilinear pattern at  $4.25 \pm 0.04$  kN (green line in Figure 8). The stiffness of the  $\theta$ °/ $\theta$ 0° rectilinear pattern  $0.98 \pm 0.01$  kN/mm, while the concentric pattern is stiffer at  $1.07 \pm 0.01$  kN/mm. The bulk structure closely matches

**Figure 8** Representative experimental load versus deflection responses for the optimized geometries with various infill patterns



the failure load and stiffness of the  $0^{\circ}/90^{\circ}$  rectilinear pattern at  $4.20 \pm 0.01$  kN and  $1.02 \pm 0.01$  kN/mm, respectively.

Representative experimental load-deflection curves of the  $0^{\circ}/90^{\circ}$  optimized structure with a varying number of shells (i.e. perimeters) are displayed in Figure 9. It is observed that the presence of shells increases the failure load to  $4.7\pm0.13\,\mathrm{kN}$  and  $5.0\pm0.1\,\mathrm{kN}$ , for two and four shells, respectively. Stiffness follows a similar trend with the presence of shells increasing the stiffness of the  $0^{\circ}/90^{\circ}$  rectilinear path from  $0.98\pm0.01\,\mathrm{kN/mm}$  to  $1.08\pm0.00\,\mathrm{kN/mm}$  and  $1.09\pm0.01\,\mathrm{kN/mm}$ , for two and four shells, respectively. The stiffness and failure loads for all tested structures are summarized in Figures 10 and 11, respectively, as well as in Table 4.

**Figure 9** Representative experimental load versus deflection responses for the 0°/90° optimized geometry with varying number of shells (i.e. perimeters)

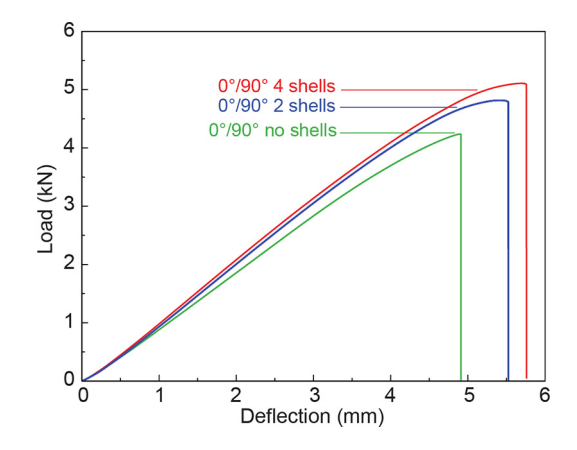
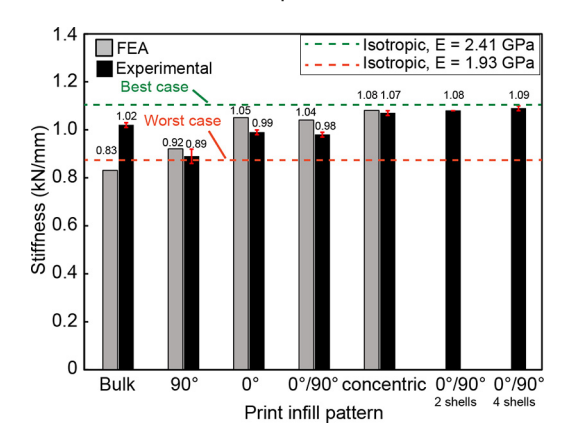
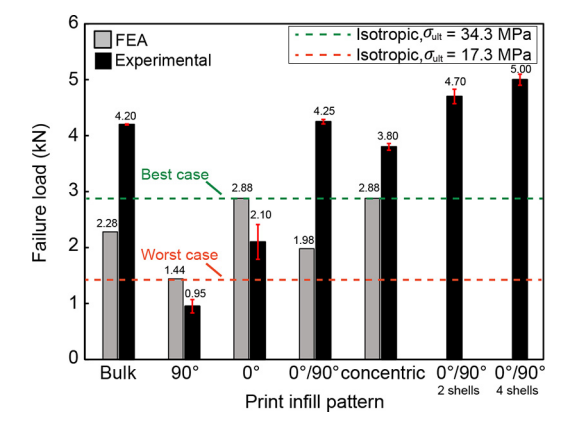


Figure 12 shows representative structures after mechanical testing. The region where failure occurred first is highlighted by a red box. A waterjet-cut structure provides a baseline for comparison of the various failure modes observed in the printed structures (Figure 12a). Failure of the bulk structure initiates at the bottom face just adjacent to the node where the inclined truss members intersect the bottom members. Both of the unidirectional infill patterns (Figures 12b–c), the 90° and 0° rectilinear patterns, fail along the printed interface in one of the inclined struts, while the 0°/90° rectilinear infill patterns all fail at the same location as the bulk waterjet-cut specimen (Figures 12d, f–g). The concentric infill pattern (Figure 12e) fails along the bottom edge of the structure at the location of the slicing-related internal pore. Failure then

**Figure 10** Numerical and experimental comparison of structural stiffness for the bulk and each infill pattern



**Figure 11** Numerical and experimental comparison of failure load for the bulk and each infill pattern



propagates along the central printed interface to one of the nodes of the structure.

#### 4.4 Numerical results

Figures 10 and 11 show a comparison between the numerical and experimental values of stiffness and failure load, respectively, along with upper and lower numerical bounds defining best-case and worst-case isotropic models. The numerically-determined stiffnesses for each infill pattern approximation are as follows, from lowest to highest: Bulk (0.83 kN/mm), 90° rectilinear (0.92 kN/mm), 0°/90° rectilinear (1.04 kN/mm), 0° rectilinear (1.05 kN/mm) and concentric (1.08 kN/mm). The upper (best-case, in green) and lower (worst-case, in orange) isotropic bounding cases resulted in stiffness values of 1.10 kN/mm and 0.87 kN/mm, respectively. Failure loads for each simulation were identified as follows, from lowest to highest: 90° rectilinear (1.44 kN), 0°/90° rectilinear (1.98 kN), Bulk (2.28 kN), 0° rectilinear (2.88 kN) and concentric (2.88 kN). The isotropic best-case and worstcase bounding cases were determined to have a failure load of 2.88 kN and 1.44 kN, respectively.

The calculated stress fields within the geometries were very similar for all material property sets. Representative fields are shown in Figures 13–14 for the isotropic best-case and  $0^{\circ}$  rectilinear cases, respectively. The stress contours were taken at the load increment at which failure was numerically predicted to occur for each case, as shown in Figure 11. Because failure was observed to occur in tension rather than compression, the color scheme was chosen to highlight only tensile stresses. The stress contours show the direct stresses in the global coordinate system, normalized by the appropriate directional ultimate strength, while the shear fields were all normalized by the lower measured shear strength ( $\tau_{21,ult} = 23.0 \, \text{MPa}$ ).

For all cases investigated by FEA, failure is predicted to occur due to tensile stresses at the bottom face near the intersection of the internal struts. In addition, shear stress is relatively low, with the highest levels approaching 50%–75% of the ultimate shear strength near the intersection of the internal struts. In general,  $\tilde{\sigma}_{yy} = \frac{\sigma_{yy}}{\sigma_{11,uh}}$  is significantly lower than  $\tilde{\sigma}_{xx} = \frac{\sigma_{xx}}{\sigma_{11,uh}}$  and only one of the internal struts in the half-beam model experiences tension in the y-direction (blue and green contours in Figures 13b and 14b). The principal stress directions remain approximately tangent to the geometric boundaries of the structure (Figures 13d and 14d) and very closely match the concentric infill pattern (Figure 5).

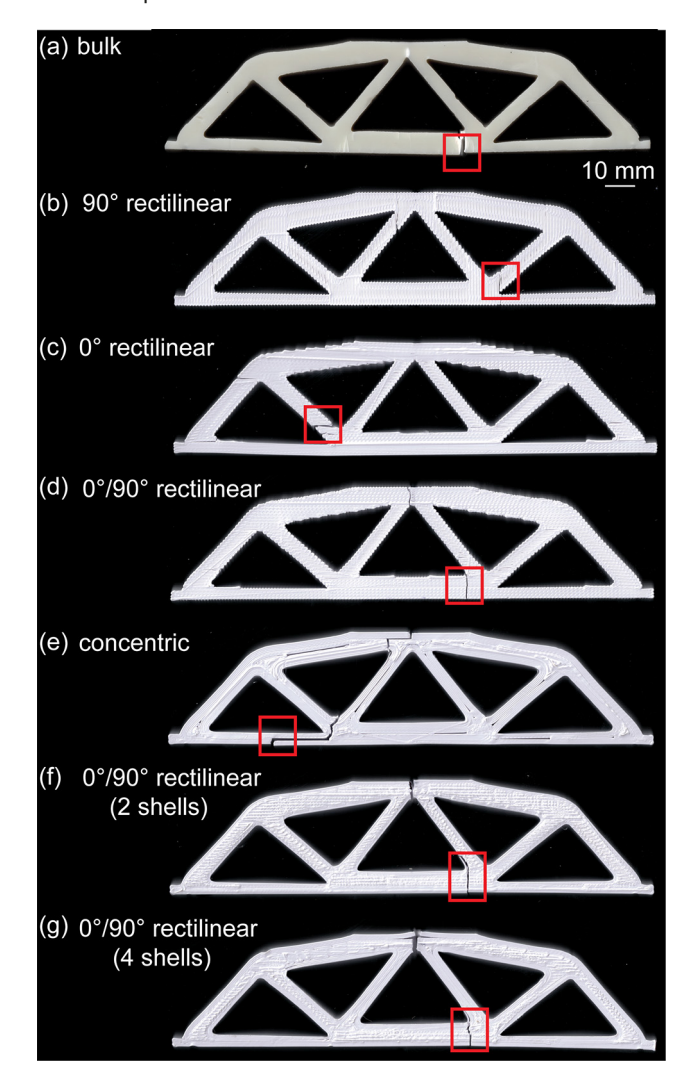
# 5. Analysis and discussion

From the experimental results, it is clear that the choice of infill pattern has a significant effect on the mechanical performance of the printed structure. In particular, the measured stiffness of

Table 4 Mechanical properties of optimized structures

Infill pattern	Bulk	90° rectilinear	0° rectilinear	0°/90° rectilinear	Concentric	0°/90° two shells	0°/90° four shells
Load (KN)	4.20 + 0.01	$0.95 \pm 0.12$	2.1 ± 0.31	$4.25 \pm 0.04$	$3.8 \pm 0.06$	$4.7 \pm 0.13$	5.0 ± 0.1
Stiffness (KN/mm)	$1.02\pm0.01$	$0.89 \pm 0.03$	$0.99 \pm 0.01$	$0.98\pm0.01$	$1.07\pm0.01$	$1.08\pm0.00$	$1.09 \pm 0.01$

**Figure 12** Optical photos of representative failed structures with various infill patterns

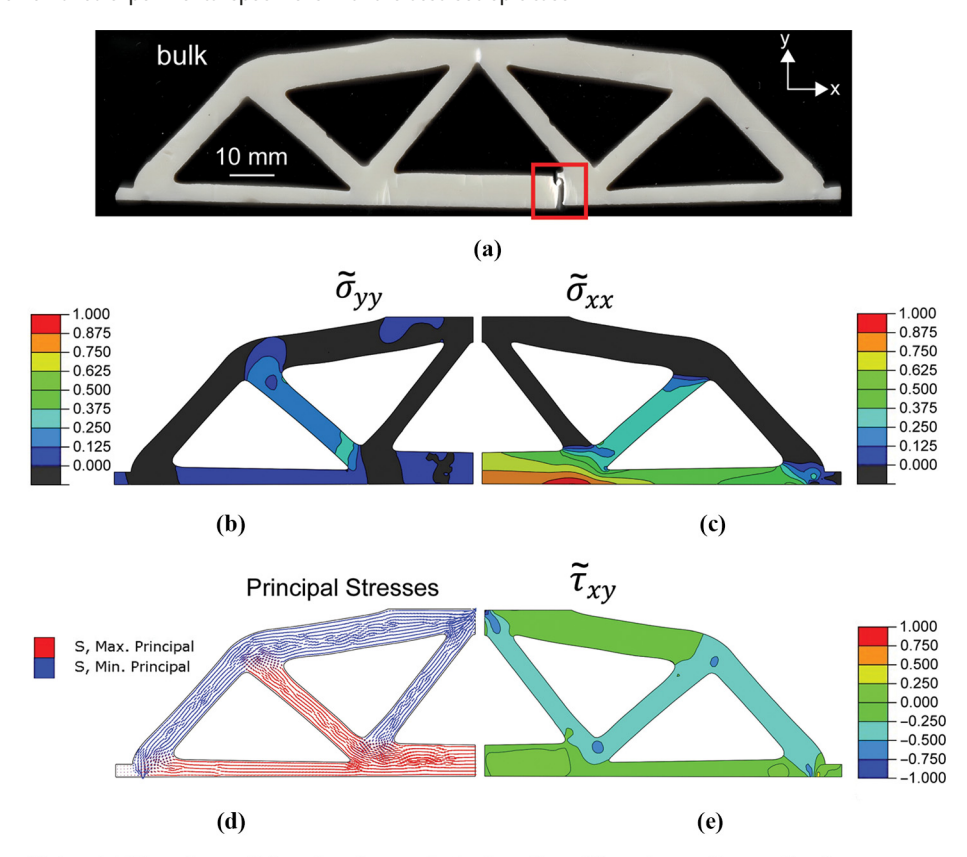


the optimized topology varied by as much as 20% without incorporating shells and up to 22% when incorporating shells (Figure 10). In comparison to stiffness, strength is significantly more sensitive to infill pattern, where the experimental failure load varied by as much as 347% between structures printed with different infill patterns without incorporating shells and up to 426% when incorporating shells (Figure 11). The measured stiffness and failure load of these structures are highly correlated to the variation in the mechanical properties between material orientations (Table 3). Herein, the tensile strength, Young's modulus, Poisson's ratio and shear strength of the 2direction specimens represented 50.44%, 80.1%, 69.44% and 84.25% of that of the 1-direction specimens, respectively. Such mechanical anisotropy in printed ABS parts has been observed in several studies. For example, Ahn et al. (2002) observed variations in the tensile and compressive strength of ABS components printed with various raster angles (i.e. infill patterns) and build directions. In addition, Ziemian et al. (2012) reported anisotropy in the tensile, compressive, flexural, impact and fatigue strength properties of printed ABS parts. In their study, the tensile strength of specimens printed at raster angles of 90°,  $45^{\circ}$  and  $+45^{\circ}/-45^{\circ}$  was found to be 56.23%, 61.45% and 74.09° of that of the 0° raster angle, respectively. Similarly, the Young's modulus was found at 74.80%, 75.09% and 77.75% of that of the 0° raster specimens, for the raster angles of 90°, 45° and +45°/-45°, respectively. Moreover, Cantrell et al. (2017) reported a variation up to 33% in the shear modulus and shear strength of printed ABS coupons with various raster and build directions; however, they found a negligible effect for the raster angle and build direction on both Young's modulus and Poisson's ratio. Generally, the foregoing studies attribute the reason behind this directional dependence or anisotropy in the mechanical properties of FFF parts to variations in the resulting mesostructure, voids-related printing, orientation of molecular chains and interfacial strength relative to the infill pattern (or raster orientation).

From the numerical results, the stiffness (Figure 10) was reliably predicted using an orthotropic material model that treats the printed layers of the structure as unidirectional composite lamina. All numerical and experimental stiffness values fell within the predicted bounds. The upper bound on stiffness (representing the optimal or maximum isotropic stiffness) was most closely approached by structures with print paths that are aligned with the contours of the geometry, i.e. the infill patterns with shells and the concentric infill patterns. This correlation is related to the minimization of strain energy in the structure, which is achieved by aligning the stiffest material direction with the principal stress direction (Pedersen, 1989). In addition, strength was not accurately predicted by the simplistic maximum stress failure criteria applied to elastic simulations (Figure 11). In the  $90^{\circ}$  and  $0^{\circ}$  rectilinear cases, experimental failure loads are 34% and 27% lower than numerical predictions, while in the remaining cases, experimental strengths are significantly higher than numerical predictions, including the isotropic best case prediction.

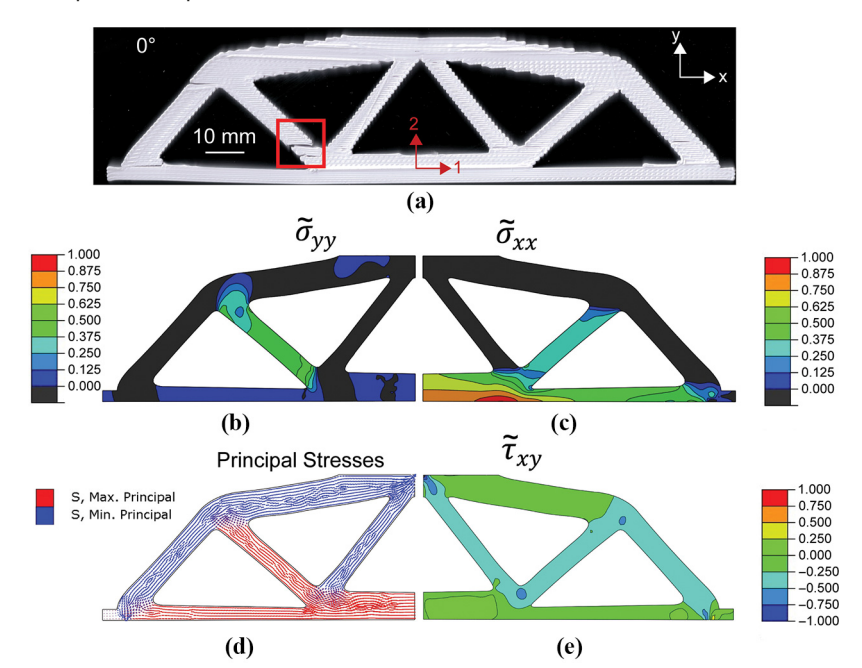
One potential reason for the observed discrepancies is the fact that plasticity is not included in the numerical simulations, even though considerable plasticity is observed in the tensile specimens prior to failure along the print direction. We believe this may be why the experimental strength is higher than the numerically-predicted strength for the 0°/90° pattern, concentric pattern and those patterns with shells. Additionally, our failure criterion was rather simplified and did not consider local ultimate strength as a function of local material orientation, but instead considered only the directional and shear stresses in comparison to the corresponding directional strengths. More robust criteria exist in the literature. For example, Yao et al. (2019) provide a Tsai-Hill protocol-based method of predicting the ultimate tensile strength of printed PLA as a function of printing angle. Each of these latter infill patterns lacks a single dominant weak direction and have some proportion of material-oriented such that the 1-direction is aligned with the x-direction on the bottom edge of the structure, where tensile stresses are highest. Printing settings are another factor that may have a significant impact on the observed ultimate strength of AM components. There is literature discussing the optimization of printing parameters for improving component strength. Spoerk et al. (2017) presents a parametric optimization of intra- and inter-layer cohesion for

Figure 13 Comparison of failed experimental specimens with the best isotropic case



**Notes:** (a) The primary failure location on the bottom face; (b) contours of normalized  $\sigma_{xx}$ ; (c) contours of normalized  $\sigma_{yy}$ ; (d) vector plot of the principal stresses; (e) contours of normalized  $\tau_{xy}$ 

Figure 14 Comparison of failed experimental specimens with 0° case



**Notes:** (a) The primary failure location on the internal strut; (b) contours of normalized  $\sigma_{xx}$ ; (c) contours of normalized  $\sigma_{yy}$ ; (d) vector plot of the principal stresses; (e) contours of normalized  $\tau_{xy}$ 

extrusion-based AM PLA components in which the effects of printing temperature, layer thickness and design and rheological properties are evaluated.

In addition, because the tensile specimens were water-jet cut, the effect of surface roughness or stair-stepping, is not reflected in the transverse strength values used to identify failure in the numerical simulations. The effective transverse strength in the printed structures may be considerably lower, due to the surface texture that results from printing (Figures 3b-d). As the stair-stepping has a high stress concentration factor (Rodet and Colton, 2003), the struts or the sections of the printed structure that exhibit curved features (Figures 3b-d) can be weaker than the rest of the structure under mechanical loading. Therefore, premature failure would most likely initiate in these regions, as observed for the 90° and 0° rectilinear cases (Figures 11 and 12b-c). Researchers in the field found that decreasing the layer height or thickness can minimize the stairstepping effect; however, that cannot eliminate it (Ayrilmis, 2018). However, the utilization of multidirectional print orientations within a single object was shown to reduce this effect (Ding et al., 2016; Zhao et al., 2018). In our case, this can be observed with the  $0^{\circ}/90^{\circ}$  rectilinear path, in which an improved mechanical behavior was achieved (Figure 8). In addition, the incorporation of reinforcement shells around the printed object act to reduce the stair-stepping effect and to improve the mechanical performance by shifting the stress away from the interfaces between layers (Kubalak et al., 2018; Huang and Singamneni, 2015). This was indeed the case for the  $0^{\circ}/90^{\circ}$ cases with shells (Figure 9). Although the concentric path can be thought of as a structure with multiple reinforcement shells, the associated stress-concentrating pores (Figures 5a and 12e) at which the structure failed prematurely (Ahn et al., 2002). Place restrictions on achieving optimal performance with the concentric pattern.

Despite the observed shortcomings in predicting the strength, the elastic stress fields can be useful in rationalizing the observed failure mechanisms in the printed structures (Figures 13 and 14). For example, based on the FEA, we would expect the  $\theta^{\circ}$  rectilinear pattern to fail in tension along the lower edge of the structure, where the tensile stresses are highest and we might expect the measured strength to be higher than the predicted strength, based on the plasticity argument presented above. However, the inclined strut where failure does occur supports tensile stress in the 2-direction that is  $\sim 60\%$  that of the failure stress of the printed, water cut tensile specimens. We anticipate that printed surface features could reduce the actual failure stress to below 60% of the intrinsic strength in the 2-direction.

Other design choices that could potentially affect the performance of any printed topology include, but are not limited to, layer thickness, air gap (i.e. spacing between roads), infill density, nozzle temperature, infill print speed, plus others. Researchers have experimentally investigated the effects of such parameters on the mechanical anisotropy of printed FFF components (Baptista et al., 2020; Turner et al., 2014; Domínguez-Rodríguez et al., 2018). It is worth highlighting that the design of optimal topologies can be further complicated when fibers and/or other filler materials are incorporated into the base polymeric material. Such complications could arise from filler orientations relative to the

print path, fiber-matrix bonding, road-to-road adhesion and resulting texture. These topics are the subject of ongoing research.

# 6. Conclusions

In this work, we have investigated the effects of discrete infill patterns on the strength, stiffness and failure modes of a 3D-printed beam structure identified by TO for compliance minimization. The choice of infill pattern was shown to be a major factor in determining the mechanical behavior of the optimized, printed topology, especially the strength and mode of failure. Anisotropy inherent to printed ABS material, along with print-related artifacts such as pores and surface roughness contributed to variations in stiffness of the optimized topology up to 22% and in failure load up to 426% between structures printed with different infill patterns. The incorporation of perimeters with rectilinear infill considerably improved the mechanical performance of the printed topology and resulted in a higher geometric fidelity.

In addition, we used elastic FE analyzes wherein individual unidirectional printed layers were represented by orthotropic composite plies with properties representative of the axial and transverse properties of the printed material. Using this approach, the stiffness of printed structures was well-predicted by numerical simulations for a variety of infill pattern choices. A straightforward maximum stress criterion was not sufficient to predict the strength of the printed structures from the elastic simulations.

This work highlights the need to pursue a deeper understanding of the effects of the design choices that must be made between the generation of an "optimal" design and the realization of that design using material extrusion AM. The results presented to establish a benchmark that can be used to guide the development of emerging manufacturing-oriented TO protocols that incorporate directionally-dependent, process-specific material properties for AM of polymers, composites and hybrid structures.

#### References

Agarwala, M.K., Jamalabad, V.R., Langrana, N.A., Safari, A., Whalen, P.J. and Danforth, S.C. (1996), "Structural quality of parts processed by fused deposition", *Rapid Prototyping Journal*, Vol. 2 No. 4, pp. 4-19.

Ahn, S.H., Montero, M., Odell, D., Roundy, S. and Wright, P. K. (2002), "Anisotropic material properties of fused deposition modeling ABS", *Rapid Prototyping Journal*, Vol. 8 No. 4, pp. 248-257.

Allaire, G., Jouve, F. and Michailidis, G. (2016), "Thickness control in structural optimization via a level set method", *Structural and Multidisciplinary Optimization*, Vol. 53 No. 6, pp. 1349-1382.

Allaire, G., Jouve, F. and Toader, A.M. (2004), "Structural optimization using sensitivity analysis and a level-set method", *Journal of Computational Physics*, Vol. 194 No. 1, pp. 363-393.

Andreassen, E., Clausen, A., Schevenels, M., Lazarov, B.S. and Sigmund, O. (2011), "Efficient topology optimization in

- MATLAB using 88 lines of code", Structural and Multidisciplinary Optimization, Vol. 43 No. 1, pp. 1-16.
- Ayrilmis, N. (2018), "Effect of layer thickness on surface properties of 3D printed materials produced from wood flour/PLA filament", *Polymer Testing*, Vol. 71, pp. 163-166.
- Baptista, R., Guedes, M., Pereira, M., Maurício, A., Carrelo, H. and Cidade, T. (2020), On the Effect of Design and Fabrication Parameters on Mechanical Performance of 3D Printed PLA Scaffolds, Bioprinting, p. 96.
- Bellini, A. and Güçeri, S. (2003), "Mechanical characterization of parts fabricated using fused deposition modeling", *Rapid Prototyping Journal*, Vol. 9 No. 4, pp. 252-264.
- Bendsøe, M.P. (1989), "Optimal shape design as a material distribution problem", *Structural Optimization*, Vol. 1 No. 4, pp. 193-202.
- Bendsøe, M.P. and Kikuchi, N. (1988), "Generating optimal topologies in structural design using a homogenization method", Computer Methods in Applied Mechanics and Engineering, Vol. 71 No. 2, pp. 197-224.
- Bendsøe, M.P. and Sigmund, O. (2004), "Topology Optimization – Theory, Methods, and Applications", Methods, and Applications, Springer, Springer-Verlag, Berlin Heidelberg.
- Calvert, P., Lin, T.L. and Martin, H. (1997), "Extrusion freeform fabrication of chopped-fibre reinforced composites", *High Performance Polymers*, Vol. 9 No. 4, pp. 449-456.
- Cantrell, J.T., Rohde, S., Damiani, D., Gurnani, R., Disandro, L., Anton, J., Young, A., Jerez, A., Steinbach, D. and Kroese, C. (2017), "Experimental characterization of the mechanical properties of 3D-printed ABS and polycarbonate parts", *Rapid Prototyping Journal*, Vol. 23 No. 4.
- Cheng, L., Zhang, P., Biyikli, E., Bai, J. and Robbins, J., T.O., A. (2017), "Efficient design optimization of variable-density cellular structures for additive manufacturing: theory and experimental validation", *Rapid Prototyping Journal*, Vol. 23 No. 4, pp. 660-677.
- Compton, B.G. and Lewis, J.A. (2014), "3D-printing of lightweight cellular composites", *Advanced Materials*, Vol. 26 No. 34, pp. 5930-5935.
- Deaton, J.D. and Grandhi, R.V. (2014), "A survey of structural and multidisciplinary continuum topology optimization: post 2000", *Structural and Multidisciplinary Optimization*, Vol. 49 No. 1, pp. 1-38.
- Ding, D., Pan, Z., Cuiuri, D., L.I., H., Larkin, N. and VAN Duin, S. (2016), "Automatic multi-direction slicing algorithms for wire based additive manufacturing", *Robotics and Computer-Integrated Manufacturing*, Vol. 37, pp. 139-150.
- Domínguez-Rodríguez, G., Ku-Herrera, J. and Hernández-Pérez, A. (2018), "An assessment of the effect of printing orientation, density, and filler pattern on the compressive performance of 3D printed ABS structures by fuse deposition", The International Journal of Advanced Manufacturing Technology, Vol. 95 Nos 5/8, pp. 1685-1695.
- Duty, C.E., Kunc, V., Compton, B.G., Post, B.K., Erdman, D., Smith, R.J., Lind, R., Lloyd, P. and Love, L.J. (2017), "Structure and mechanical behavior of big area additive manufacturing (BAAM) materials", *Rapid Prototyping Journal*, Vol. 23 No. 1, pp. 181-189.

- Gaynor, A.T., Meisel, N.A., Williams, C.B. and Guest, J.K. (2014), "Multiple-material topology optimization of compliant mechanisms created via PolyJet three-dimensional printing", Journal of Manufacturing Science and Engineering, Vol. 136 No. 6, p. 61015.
- Gersborg-Hansen, A., Bendsøe, M.P. and Sigmund, O. (2006), "Topology optimization of heat conduction problems using the finite volume method", *Structural and Multidisciplinary Optimization*, Vol. 31 No. 4, pp. 251-259.
- Gibson, I., Rosen, D.W. and Stucker, B. (2014), Additive Manufacturing Technologies, Springer.
- Grejtak, T. Jia, X. Cunniffe, A.R. Shi, Y. Babuska, T.F. Pack, R.C. Vermaak, N. Compton, B.G. and Krick, B.A. (2020), "Whisker orientation controls wear of 3D-printed epoxy nanocomposites", Additive Manufacturing, p. 101515.
- Hmeidat, N.S., Kemp, J.W. and Compton, B.G. (2018), "High-strength epoxy nanocomposites for 3D printing", *Composites Science and Technology*, Vol. 160, pp. 9-20.
- Hmeidat, N.S., Pack, R.C., Talley, S.J., Moore, R.B. and Compton, B.G. (2020), Mechanical Anisotropy in Polymer Composites Produced by Material Extrusion Additive Manufacturing. Additive Manufacturing, Vol. 34, p. 101385.
- Huang, B. and Singamneni, S.B. (2015), "Curved layer adaptive slicing (CLAS) for fused deposition modelling", *Rapid Prototyping Journal*, Vol. 21 No. 4.
- Jiang, D., Hoglund, R. and Smith, D.E. (2019), "Continuous fiber angle topology optimization for polymer composite deposition additive manufacturing applications", *Fibers*, Vol. 7 No. 2, p. 14.
- Kubalak, J.R., Wicks, A.L. and Williams, C.B. (2018), "Using multi-axis material extrusion to improve mechanical properties through surface reinforcement", *Virtual and Physical Prototyping*, Vol. 13 No. 1, pp. 32-38.
- Langelaar, M. (2016), "Topology optimization of 3D selfsupporting structures for additive manufacturing", Additive Manufacturing, Vol. 12, pp. 60-70.
- Lazarov, B.S., Wang, F. and Sigmund, O. (2016), "Length scale and manufacturability in density-based topology optimization", *Archive of Applied Mechanics*, Vol. 86 Nos 1/2, pp. 189-218.
- Leary, M., Merli, L., Torti, F., Mazur, M. and Brandt, M. (2014), "Optimal topology for additive manufacture: a method for enabling additive manufacture of support-free optimal structures", *Materials & Design*, Vol. 63, pp. 678-690.
- Liu, J. and Ma, Y. (2016), "A survey of manufacturing oriented topology optimization methods", *Advances in Engineering Software*, Vol. 100, pp. 161-175.
- Liu, J. and To, A.C. (2017), "Deposition path planningintegrated structural topology optimization for 3D additive manufacturing subject to self-support constraint", Computer-Aided Design, Vol. 91, pp. 27-45.
- Liu, J., Gaynor, A.T., Chen, S., Kang, Z., Suresh, K., Takezawa, A., Li., L., Kato, J., Tang, J. and Wang, C.C. (2018), "Current and future trends in topology optimization for additive manufacturing", *Structural and Multidisciplinary Optimization*, Vol. 57 No. 6, pp. 2457-2483.
- Liu, K. and Tovar, A. (2014), "An efficient 3D topology optimization code written in matlab", *Structural and Multidisciplinary Optimization*, Vol. 50 No. 6, pp. 1175-1196.

- Liu, J. and Yu, H. (2017), "Concurrent deposition path planning and structural topology optimization for additive manufacturing", *Rapid Prototyping Journal*, Vol. 23 No. 5, pp. 930-942.
- Ma, Z.D., Kikuchi, N. and Hagiwara, I. (1993), "Structural topology and shape optimization for a frequency response problem", *Computational Mechanics*, Vol. 13 No. 3, pp. 157-174.
- Pedersen, P. (1989), "On optimal orientation of orthotropic materials", *Structural Optimization*, Vol. 1 No. 2, pp. 101-106.
- Peng, J., Lin, T.L. and Calvert, P. (1999), "Orientation effects in freeformed short-fiber composites", Composites Part A: Applied Science and Manufacturing, Vol. 30 No. 2, pp. 133-138.
- Pierson, H., Celik, E., Abbott, A., DE Jarnette, H., Gutierrez, L.S., Johnson, K., Koerner, H. and Baur, J. (2019), "Mechanical properties of printed epoxy-carbon fiber composites", *Experimental Mechanics*, pp. 1-15.
- Rodet, V. and Colton, J.S. (2003), "Properties of rapid prototype injection mold tooling materials", *Polymer Engineering & Science*, Vol. 43 No. 1, pp. 125-138.
- Shofner, M., Lozano, K., Rodríguez-Macías, F. and Barrera, E. (2003), "Nanofiber-reinforced polymers prepared by fused deposition modeling", Journal of Applied Polymer Science, Vol. 89 No. 11, pp. 3081-3090.
- Sigmund, O. and Maute, K. (2013), "Topology optimization approaches", *Structural and Multidisciplinary Optimization*, Vol. 48 No. 6, pp. 1031-1055.
- Spoerk, M., Arbeiter, F., Cajner, H., Sapkota, J. and Holzer, C. (2017), "Parametric optimization of intra-and inter-layer strengths in parts produced by extrusion-based additive manufacturing of poly (lactic acid)", *Journal of Applied Polymer Science*, Vol. 134 No. 41, pp. 45401
- Standard, A. (2005), "d5379/d5379m, 2005", Standard Test Method for Shear Properties of Composite Materials by the V-Notched Beam Method, West Conshohocken, PA.
- Standard, A. (2010), D638: Standard Test Method for Tensile Properties of Plastics, ASTM International, West Conshohocken (PA).
- Sun, Q., Rizvi, G., Bellehumeur, C. and Gu, P. (2008), "Effect of processing conditions on the bonding quality of FDM polymer filaments", *Rapid Prototyping Journal*, Vol. 14 No. 2, pp. 72-80.

- Tekinalp, H.L., Kunc, V., Velez-Garcia, G.M., Duty, C.E., Love, L.J., Naskar, A.K., Blue, C.A. and Ozcan, S. (2014), "Highly oriented carbon fiber-polymer composites via additive manufacturing", *Composites Science and Technology*, Vol. 105, pp. 144-150.
- Trigg, E.B., Hmeidat, N.S., Smieska, L.M., Woll, A.R., Compton, B.G. and Koerner, H. (2021), Revealing Filler Morphology in 3D-Printed Thermoset Nanocomposites by Scanning Microbeam X-Ray Scattering. Additive Manufacturing, Vol. 37, p. 101729.
- Turner, B.N., Strong, R. and Gold, S.A. (2014), "A review of melt extrusion additive manufacturing processes: i. Process design and modeling", *Rapid Prototyping Journal*,
- Wang, M.Y., Wang, X. and Guo, D. (2003), "A level set method for structural topology optimization", Computer Methods in Applied Mechanics and Engineering, Vol. 192 Nos 1/2, pp. 227-246.
- Wu, J., Aage, N., Westermann, R. and Sigmund, O. (2017), "Infill optimization for additive manufacturing – approaching bone-like porous structures", *IEEE Transactions* on Visualization and Computer Graphics, Vol. 24 No. 2, pp. 1127-1140.
- Yang, K.K., Zhu, J.H., Wang, C., Jia, D.S., Song, L.L. and Zhang, W.H. (2018), "Experimental validation of 3D printed material behaviors and their influence on the structural topology design", *Computational Mechanics*, Vol. 61 No. 5, pp. 581-598.
- Yao, T., Deng, Z., Zhang, K. and Li, S. (2019), "A method to predict the ultimate tensile strength of 3D printing polylactic acid (PLA) materials with different printing orientations", *Composites Part B: Engineering*, Vol. 163, pp. 393-402.
- Zhao, H.M., He, Y., Fu., J.Z. and Qiu, J.J. (2018), "Inclined layer printing for fused deposition modeling without assisted supporting structure", *Robotics and Computer-Integrated Manufacturing*, Vol. 51, pp. 1-13.
- Ziemian, C., Sharma, M. and Ziemian, S. (2012), "Anisotropic mechanical properties of ABS parts fabricated by fused deposition modelling", *Mechanical Engineering*, Vol. 23.

#### **Corresponding author**

Brett Compton can be contacted at: bcompto1@utk.edu